Science Advances
AAAS

advances.sciencemag.org/cgi/content/full/4/12/eaau9711/DC1

Supplementary Materials for

In situ recombination junction between p-Si and TiO_2 enables high-efficiency monolithic perovskite/Si tandem cells

Heping Shen, Stefan T. Omelchenko, Daniel A. Jacobs, Sisir Yalamanchili, Yimao Wan, Di Yan, Pheng Phang, The Duong, Yiliang Wu, Yanting Yin, Christian Samundsett, Jun Peng, Nandi Wu, Thomas P. White, Gunther G. Andersson, Nathan S. Lewis*, Kylie R. Catchpole*

*Corresponding author. Email: nslewis@caltech.edu (N.S.L.); kylie.catchpole@anu.edu.au (K.R.C.)

Published 14 December 2018, *Sci. Adv.* **4**, eaau9711 (2018)
DOI: 10.1126/sciadv.aau9711

This PDF file includes:

Supplementary text

Single-junction perovskite solar cell performance

The thickness of perovskite was controlled by varying the precursor concentration and the spinning speed. The three approaches produced perovskite films with thickness of ~470 nm (Approach 1), ~380 nm (Approach 2) and ~310 nm (Approach 3), respectively (fig. S1D-F). We then tested the perovskite film quality fabricated with different approaches by incorporating them in the single-junction PSCs with FTO as the substrate, gold as the rear contact, and an optimized solution-based TiO_2 as the compact layer. The corresponding photovoltaic metrics of the devices with each perovskite layer thickness are displayed in fig. S3. With thinner perovskite film in devices, we achieved almost unchanged V_{oc} and slightly increased FF, while J_{sc} was reduced as expected. To reach current matching between two subcells, a relatively thin perovskite film is required based on the present composition with a bandgap of ~1.63 eV [13]. Therefore, we used the recipe that produces a 310 nm-thick perovskite film in the tandem device. Though different substrates were used, planar Si for the tandem device and FTO for the single-junction PSC, the perovskite film fabricated with the same process exhibits similar perovskite film thickness. However, the perovskite film deposited on the ultra-flat ALD-TiO_2 coated Si substrate (fig. S2C) is more uniform and flat than that deposited on FTO substrate (fig. S2D), which accordingly benefits the photovoltaic performance. This thus contributes partially to the high FF yield of the perovskite/Si tandem device beyond the extraordinary contact behaviour between p^+-Si and TiO_2.

Optical simulation indicates the highest perovskite/Si tandem efficiencies can be achieved using perovskite with a bandgap in the range of ~1.7 – 1.8 eV for both 4-T and 2-T tandem configurations [21]. However, at present, high band gap perovskites show a greater difference between the band gap and cell V_{oc} than lower band gap perovskites. For instance, the smallest V_{oc} deficit achieved so far is ~0.39 V for the 1.63 eV mixtures [7], but is as large as ~0.65 V for the other high-efficiency high bandgap perovskite systems [22] and has only recently been reduced to ~0.47 V for the 1.72 eV perovskite [23]. Therefore, in its current state of development, one should not expect much of a gain in tandem voltage from using the high-bandgap mixture. Furthermore, the 1.63 eV perovskites have passed the industry-relevant stability tests [8, 12], whereas the high-bandgap mixtures remain unproven. The optimal bandgaps are calculated on the basis of current matching, but do not typically account for optical losses that can disproportionally reduce the current in the top cell, thereby requiring a compensation in bandgap. These optical losses are substantial even in the latest tandem designs [8, 12].

Single-junction Si solar cell performance

The photovoltaic performance of our single-junction homojunction Si solar cells is shown in fig. S4C, whereas the behaviour of the passivating-contact heterojunction cells is shown in fig. S5E. The observed efficiencies reflect the different requirements of tandem sub-cells and standalone Si devices. For instance, a flat Si front surface was used in our tandems to enhance compatibility with solution processing of the perovskite sub-cell. Anti-reflection was dealt with in our tandems by adding a front-side foil, and is naturally lower with the perovskite top-cell included due to reduced refractive index contrast. Simply attaching a textured foil onto our Si cell resulted in an absolute J_{sc} increase of ~3.6 $mAcm^{-2}$, producing an efficiency of ~17.5% from the poly-Si solar cell (fig. S5E). The observed standalone efficiencies are thus primarily a result of suboptimal optical characteristics of these devices and thus are not representative of the performance of the sub-cells in our tandem devices.

The pseudo-FF of the poly-Si subcell was ~0.810 (pseudo *J-V* curve in fig. S5E), considerably higher than the true FF, indicating that further improvement can be realized by reducing series resistance. The contact resistivity of the TiO_2/poly-Si interface was as low as ~150 mΩcm^2 (fig. S5D), hence only constituting a small proportion of the total series resistance of ~1.8 Ωcm^2 (fig. S5E), this parasitic resistance likely originates from the rear-side contacts. In this connection it is worth noting that for perovskite/Si tandems the issue of series resistance is much less severe for perovskite/Si tandems than it would be for single-junction Si cells (by a factor of ~5 [39]), due to the higher voltage and lower current of the tandems relative to single-junction devices.

Due to the voltage gain of the passivating-contact poly-Si subcell (~665 mV) as compared to the homojunction subcell (~600 mV using the low contact-resistivity TDMAT-ALD TiO_2), higher tandem voltage was observed based on the former bottom subcell. Lifetime tests indicated that an implied V_{oc} as high as ~700 mV can be reached with the present poly-Si films front designs (fig. S5C). With proper optimization, such as tuning the doping profile and thickness of the poly-Si, as well as the SiO_2/poly-Si interface, the open-circuit voltage could exceed 720 mV [18, 24], falling in the regime that can be considered as state-of-the-art [12]. Notably, increases in the Si sub-cell voltage do not produce as much improvement in absolute efficiency for a tandem structure as would be observed for single-junction Si cells, due to a factor of ~2 reduction in the collected current.

XRD analysis of different TiO_2 films

XRD patterns in fig. S2A indicates that the as-deposited TiO_2 film is amorphous, while it becomes crystallized after annealing at 400 °C. This is cosistent with the results from STEM measurement (Fig. 1D and fig. S1B, C). All titania films from different precursors (after annealing at 400 °C for 20 min) were polycrystalline anatase with no evidence of any rutile phases (fig. S2B).

Perovskite and perovskite/Si tandem device stability (fig. S6 – fig. S9)

The sensitivity of perovskite solar cells to a range of external agents including moisture, heat, oxygen, bias, UV light, etc. is well recognized. Though the stability issue of the perovskite solar cells has not been ultimately addressed, substantial progress has been achieved in the last few years through efforts devoted to compositional engineering [7], material choices (for instance, using inorganic charge transport materials), interfacial engineering and encapsulation [8]. In terms of stability, fully inorganic perovskite materials are promising candidates to fabricate stable perovskite top cells. $CsPbI_3$ in its cubic phase has a particularly suitable bandgap. However, the efficiencies of inorganic devices are still far away from satisfactory, with a highest efficiency of ~10.74% [41] to date. By contrast multiple-cation hybrid perovskite materials have been consistently reported with state-of-the-art efficiencies, and can be engineered to exhibit respectable stability [7, 22]. For instance, devices based on Cs/FA binary perovskites have passed the damp heat test (85 °C in 85% relative humidity) with encapsulation [8, 12]. The Cs/FA/MA triple cation perovskite solar cell has shown impressive stability with the un-encapsulated device retaining 94% of peak efficiency despite 1,000 hours of continuous operation in ambient air conditions (relative humidity of 10–20%).[25] Quadruple cation (Rb/Cs/MA/FA) perovskites have been reported to exhibit superior photovoltaic performance, as well as an impressively small loss-in-potential of 0.39 V [7, 22], and stress testing of these cells has exceeded industrial standards (the device

retained 95% of its initial performance after tracking at V_{MPP} under illumination at 85°C for over 500 h) [7].

In this work we used a quadruple-cation perovskite with a composition of $Cs_{0.05}Rb_{0.05}FA_{0.765}MA_{0.135}PbI_{2.55}Br_{0.45}$. The inorganic cations, Cs and Rb, both appear to benefit the device efficiency. Rb was found to facilitate crystallization, resulting in high-quality perovskite films with better homogeneity and suppressed impure phases [7]. MA has benefits in terms of reducing the large discrepancy in size between FA and Cs, slowing down the crystallisation process to achieve defect-free films, and facilitating the formation of α-phase perovskite. We also note that MA was included in the perovskite film that resulted in the reported record single-junction solar cell with good air stability.[42] In our work, its concentration was kept low (13.5%) due to its higher heat sensitivity than the other cations. FA was chosen as the primary cation component (76.5%) due to its superior but still imperfect stability towards moisture and heat.

(a) Damp heat test (85 °C in 85% relative humidity)

As the perovskite subcell is the major unstable component in the tandem device, we therefore first stress-tested the stability of the single-junction perovskite solar cell as has been done previously in the work by McGehee et al.[8] and Sahli et al. [12]. We investigated the stability with respect to heat and moisture by performing the damp heat test according to the testing protocol 61215 defined in the International Electrochemical Commission (IEC) (85°C in 85% relative humidity). Spiro-OMeTAD based perovskite solar cells show poor thermal stability as Spiro-MeOTAD has a glass transition temperature at around 85 °C, above which the hole mobility deteriorates markedly [43]. In contrast, PTAA results in substantially improved thermal stability of perovskite solar cells. [7, 44] The best-performing perovskite/Si tandem is based on PTAA HTL, so we performed the damp heat tests on semi-transparent perovskite solar cells with PTAA as the HTL. The devices were encapsulated utilizing a butyl rubber edge seal.

In detail, the encapsulated solar cells are aged in an 85 ◦C and 85% relative humidity chamber in the dark. The cells were then taken out from the chamber after every tens- (at early stage of the aging process) or hundreds of hours (at late stage of the aging process), and cooled down to room temperature for photovoltaic performance measurement. The solar cells were measured with a scanning rate of 50 mV/s without preconditioning. With the relatively small initial hysteresis, these perovskite solar cells showed marginal changes in the hysteresis behavior before and after aging. The photovoltaic metrics including the efficiency (fig. S6) were extracted from the reverse *J-V* scans.

The detailed evolution of their photovoltaic metrics is shown in fig. S6, indicating respectable thermal stability. With an initial absolute efficiency of 11.81%, the tested encapsulated devices maintain an efficiency of 10.52%, corresponding to ~89% of its original output after testing for > 1400 h. We note that as reported in the literature [8, 12], encapsulation resulted in device efficiency reduction (an average efficiency of over 15% before encapsulation in our work) mainly ascribed to drop in J_{sc}, as no index-matching encapsulant was present between the cell and the glass cover sheet. The heat treatment during the soldering of the wire onto the device also leads to slight reduction in V_{oc} and FF. The efficiency drop of the encapsulated device during the heat treatment is mainly caused by the FF drop, while the V_{oc} and J_{sc} underwent smaller degradation, corresponding to relative decreases of ~1.3% and 0.73% respectively. This puts these cells within a hair's breadth of passing protocol 61215, which requires 90% retained efficiency, but shows that our cells are well within the stability established by McGehee et al. [8] and the more recent tandem device by Ballif et al.[12]. We did damp heat tests for two semitransparent perovskite devices with encapsulation. Multiple

causes could contribute to the observed performance drops, including suboptimal encapsulation, degradation of the organic HTM, migration of extrinsic ions introduced from the HTM to perovskite, and metal electrode diffusion into the perovskite [25]. The utilization of MA in the perovskite composition is not considered to be the primary issue, since stability of the devices with similar quadruple cation composition have exceeded industrial standards with the assistance of polymer-encapsulation [7].

It has been widely reported that the extrinsic ion (dopant) migration from HTL to perovskite as well as Au migration to perovskite are also important contributors to the device degradation. Our encapsulated semitransparent cells used perovskite/MoO_x/PTAA/IZO/Au grid structure instead of a perovskite/PTAA/full-area Au structure, which is beneficial for eliminating both types of migration. The perovskite and PTAA are isolated by an additional MoO_x layer, which is favorable for retarding the extrinsic ion migration from the doped HTM into perovskite. Moreover, the TCO (IZO herein) effectively prohibits Au migration to the perovskite. The utilization of a Au grid also enabled a much smaller amount of Au to be utilized as compared to a full-area gold structure in opaque devices (shading of ~3%).

Overall, though PTAA HTL based PSCs show decent thermal stability, further improvement can be obtained by use of more-stable HTMs, such as p-type inorganic semiconductors, including CuPc, CuSCN, NiO_x et al. Notably, the latter two of the abovementioned alternatives have additional benefits of improved optics relative to PTAA [27], thus being promising for the construction of both highly-performing and stable tandems. At the present stage, the method of deposition of these materials needs to be optimized in terms of the selection of a solvent and mild post-treatment that does not affect the perovskites. Our tandem structure with in-situ recombination junction is compatible with the use of new HTLs.

The statistics of the photovoltaic parameter evolution of four non-encapsulated semitransparent solar cell aged at 85 °C for 24 h are shown in fig. S7, which shows a narrow distribution.

(b) Light-soaking (controlled at 60 °C)

We continued to investigate the operational stability of our perovskite devices controlled at 60 °C. Instead of encapsulating these cells, we carried out tests under N_2 atmosphere to simulate ideal isolation from moisture and oxygen. We tested our standalone perovskite solar cell under continuous full-spectrum AM 1.5 1-sun illumination (100 mW cm^{-2}), with the cell biased close to the maximum power point for 44 h. This meets the requirement of 43 KWh m^{-2} irradiation defined in IEC 61646. We tested four devices, all of which exhibit comparable stability behaviour. We show the evolution of photovoltaic metrics for one of these devices in fig. S8. The device has an efficiency of 16.03%, and retained 97.6% of its original output after 44 h light soaking. Both the V_{oc} and FF dropped by ~1.8%, while the J_{sc} increased by 1.2%. Overall, our perovskite solar cell exhibits good light-soaking stability at 60 °C.

(c) Long-term stability of perovskite/Si tandem solar cell

Though there has been a range of studies dealing with the stability of the single-junction perovskite solar cell, the stability of the tandem device, especially the light stability has only been reported in the recent work on tandem device by Ballif et al. [12] Our perovskite/Si tandem device maintained an efficiency of ~18.4% after an aging period of ~2500 h in total, including overall illumination for ~800 h, corresponding to over 80% of its original output. Notably the cell spent more than 20 h during this aging period under 1-sun illumination in air. In detail, the aging test included four stages (fig. S9). Stage 1 and Stage 3 were stress tests, entailing exposure to air, continuous illumination at full spectrum 1-sun intensity, and biasing

near the maximum power point. Stage 2 consisted of storing the devices in the dark in an N_2 cabinet, after which the cells were taken out for *J-V* characterization (1200 h). Stage 4 consisted of light/dark cycles under a constant N_2 flow (with illumination for over 800 h).

Unsurprisingly the fastest degradation occurred in the stress tests of Stage 1 and Stage 3 (fig. S9A and fig. S9C, highlighted in yellow), where moisture, oxygen and the interaction of light with these species are all potential culprits. The performance degradation under these conditions was almost linear, which is consistent with the recently published result shown for the tandem device with record efficiency. [12] However, we found that such degradation can be mostly reversed after resting the cells in the dark, as seen by the efficiency returning to ~20.4 % as compared to ~20.7% before stress testing in Fig. S9C. This indicates that irreversible chemical degradation by moisture and oxygen is a minor factor under short-term exposure to air and illumination. The interaction of light with oxygen and light-enhanced ion migration could then be the major contributors for the reduction during the stress tests. This "dark recovery" has been previously reported for single junction perovskite solar cells [45], whilst this is the first time that has been investigated on the perovskite/Si tandem. In Stage 2 (fig. S9B), with storage of the device in dark for ~1200 h, no performance recovery was observed, but the performance degradation was also relatively small (with the efficiency dropping from 21.9% to 21.4% after ~700 h aging in the dark). A further reduction to ~20.7% efficiency was observed after another ~500 h aging.

The degradation of the tandem device under illumination in N_2 atmosphere was slow over the ~800 h light/dark cycles. A 10% reduction measured from the start of each cycle (20.4% for the starting point of the first cycle and 18.4% for the seventh cycle) was observed over the full light/dark cycling test (7 cycles of approx. 120 h). This is somewhat comparable to the current record tandem cell [12], wherein an efficiency drop of ~10% during the course of ~250 h illumination was reported, although a different testing protocol and the phenomenon of dark recovery makes direct comparison difficult. Similarly, we observe clear dark recovery after comparable storage time in all the light/dark cycles. Overall, our perovskite/Si tandem exhibited respectable stability, with over 80% efficiency remaining after aging under various conditions for >2500 h.

Whilst protocols of assessing the perovskite solar cell still vary largely [45], our perovskite-based device shows promising stability after industry standard stress tests (including the damp heat test and light soaking at 60°C) and the long-term tracking of our perovskite/Si tandem device performance including over 800 h illumination and dark recovery.

The titania is on the rear side of the top-cell and is therefore almost completely shielded by the perovskite and other front-side layers that strongly absorb UV. This configuration may therefore have benefits in terms of stability, as the photocatalytic effect of TiO_2 [46] has been discussed as one of the main causes of as-prepared perovskite degradation.

XPS analysis of different annealed TiO_2 films studied in Fig.3B

From XPS measurements (fig. S11A), the TiO_2 films fabricated from different precursors exhibit mutually similar Ti 2p signals, with Ti 2p 3/2 peaks locating at 458.9-459.0 eV, which we attribute to Ti^{4+} species, with only small amount of Ti^{3+} was detected at higher binding energy. There was also no observable difference between the as-deposited and annealed samples, indicating that the changes in the oxygen vacancy concentration induced by the annealing is beyond the detection limit of our XPS measurements. Unlike the TDMAT-ALD TiO_2 and TTIP-ALD TiO_2, a considerable amount of Cl was detected for the $TiCl_4$-ALD TiO_2 films.

The work function was calculated from the secondary electron cut-off of the UPS spectrum which were individually deconvoluted with a Gaussian function that reflecting the energy resolution of the electrostatic energy analyser (explained in detail in the reference) and a Fermi distribution function describing the occupation of the electron energy states. A linear function was then fit to extract the work function, which is determined as the energy at the intersection of the linear function and the energy axis. The work function measurements in conjunction with the position of the valence band and conduction band were used to determine the ionization potential.

Low-temperature processed TiO_2/p^+-Si contact behavior and tandem device performance

We further optimized the contact resistance of unannealed TiO_2/p^+-Si samples by increasing the reactor temperature during deposition. The ALD reactor temperature was limited to ≤200 °C, which at its maximum still qualifies as "low-temperature" for most applications.

For these tests, we adopted two different p^+-Si substrates having doping densities of ~9.3×10^{19} cm^{-3} and 1.7×10^{20} cm^{-3}, respectively, to enhance the interfacial conductivity, as suggested by Shockley-Read-Hall theory. Concurrently the reactor temperature was raised to 150 °C and 200 °C from 75 °C (as in the data of Fig. 3 in the main text) for the $TiCl_4$ as precursor. The *J-V* behavior, including the extracted contact resistivity, are shown in fig. S13A for each deposition condition. Increasing either the p^+-Si doping density or the TiO_2 deposition temperature reduced the contact resistivity. TiO_2 deposited at 150 °C yielded contact resistivities of ~850 $m\Omega cm^2$ and ~450 $m\Omega cm^2$ for the low- and high- p^+-Si doped substrates, respectively. The contact resistivity was further reduced by raising the depsoition tempearture to 200 °C. Ultimately, a contact resistivity as low as ~99.6 $m\Omega cm^2$ was obtained with a deposition temperature of 200 °C in conjunction with the highest wafer doping. These results demonstrate the compatibility of this contact scheme with low-temperature processing requirements, as imposed by Si HIT cells with ultra-thin amorphous silicon layers.

UPS valence band spectra in fig. S13D indicate that titania deposited at 75 °C and 150 °C show similar work functions, while the titania deposited at 200 °C exhibited a smaller work function (~4.4 eV). IPES measurements showed a smaller separation between the fermi-level and conduction-band for the samples deposited at higher temperature (fig. S13E), with calculated separation values of ~0.4 eV, ~0.3 eV and ~0.2 eV for $TiCl_4$-ALD TiO_2 deposited at 75 °C, 150 °C and 200 °C, respectively. When the same p^+-Si was used, these data indicate a relatively larger interfacial offset of TiO_2 deposited at 200 °C (E_c, 200°C-TiO_2 of ~ 4.2 eV) as compared to that deposited at 75 °C (E_c, 75 °C-TiO_2 of ~ 4.4 eV, fig.S12). The lower contact resistivity correlates with an increase in the proportion of Ti^{3+} defects (signified by the larger shoulders in the Ti 2p core photoelectron spectra in fig. S13C), which are correlated with the intrinsic TiO_2 doping density. This correlation is consistent with the smaller separation between the fermi-level to conduction-band of the $TiCl_4$-ALD TiO_2 deposited at 200 °C.

The low contact resistivity enabled mainly by a high doping density of TiO_2 (eg. $TiCl_4$-ALD deposited 200 °C in this work, with no further heat-treatment) instead of a small interfacial offset by high work-function TiO_2 also allowed the omission of the mesoporous TiO_2 in the tandem device. In our preliminary tests, a low-temperature-processed, interlayer-free perovksite/Si tandem based on the planar perovskite top subcell was construsted using the $TiCl_4$-ALD TiO_2 deposited 200 °C. A poly-Si subcell was used as the bottom subcell in this test. The *J-V* characteristic of the device is shown in fig. S14C, exhibiting tandem voltages as high as ~1.75 V, comparable with those using the mesoporous TiO_2 layer. This behavior

indicates that the mesoporous layer is not necessary for maintaining the top-cell voltage when the work function of the compact layer is sufficiently small. The sub-optimal FF and J_{sc} could be further imrpoved by optimizing the top perovskite fabrication processess, especially wetting on the planar TiO_2 via interfacial engineering [38] and balancing the current yield of the two subcells.

Among these newly-developed TiO_2 layers, we also found the un-annealed $TiCl_4$-ALD TiO_2 deposited at 150 °C increased the lifetime of the Si wafer, to the tune of ~50 mV in implied V_{oc} (fig. S5A). The contact resisivtity for the un-annealed $TiCl_4$-ALD TiO_2 was also reasonable, ~960 mΩcm^2 (fig. S5B). This is unlikely to represent a global optimum, however, and a number of approaches are available to further improve the tradeoff between contact resistivity and passivation. In particular, TDMAT might be expected to give better performance as a precursor than the $TiCl_4$ used in these tests, as per the results in Fig. 3.

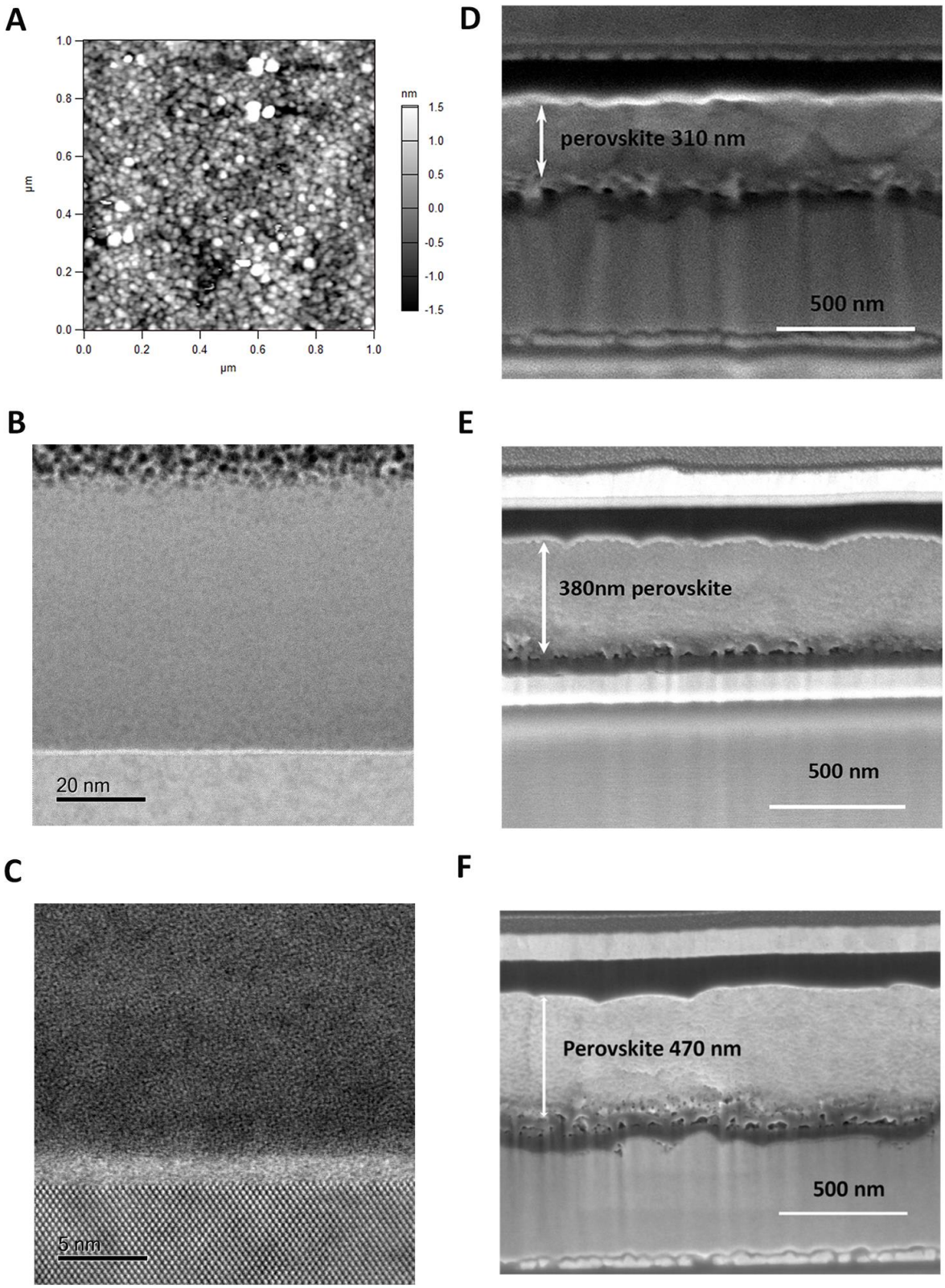

Fig. S1. Morphologies of TiO_2, cross-sectional TiO_2/Si interface, and perovskite solar cell. (**A**) AFM image of TDMAT-ALD TiO_2 on a p^+-Si substrate. (**B**) STEM and (**C**) High-resolution STEM images of the as-deposited TiO_2/p^+-Si interface using TDMAT-ALD TiO_2. (**D**-**F**) Cross-sectional SEM images of the opaque perovskite devices with different perovskite thicknesses (Note that the error bar is ±20 nm).

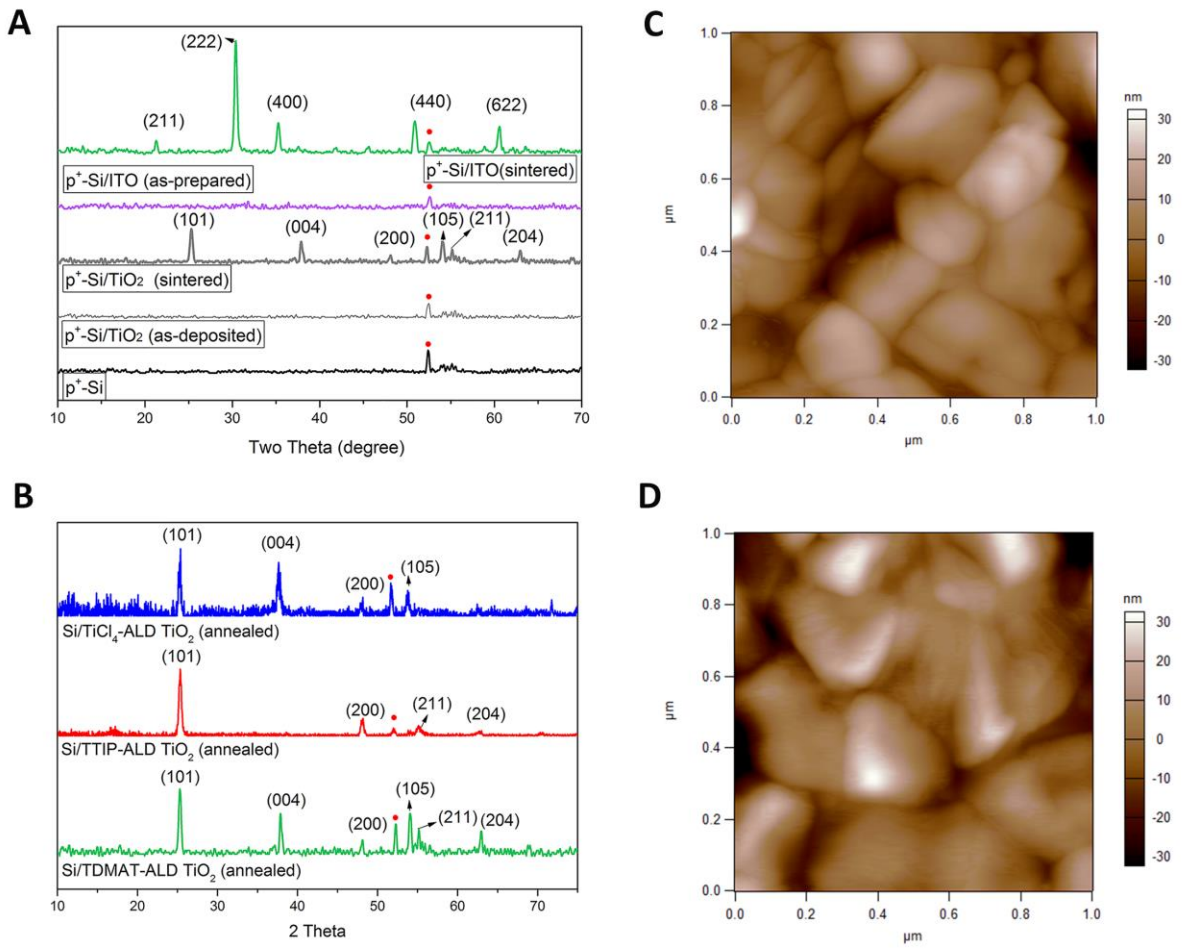

Fig. S2. XRD patterns of TiO_2 and ITO films and perovskite morphology on different substrates. GIXRD patterns of (**A**) TDMAT-ALD TiO_2 and ITO deposited on p^+-Si layer before and after annealing, and (**B**) TiO_2 fabricated from different precursors, including TDMAT, $TiCl_4$ (75°C) and TTIP. All of the samples were annealed at 400 °C under ambient conditions. AFM images of the perovskite layer on top of (**C**) an ALD TiO_2/p^+-Si substrate. The film had a RMS roughness of 9.73 nm. (**D**) FTO substrate. The film has a RMS roughness of 13.0 nm.

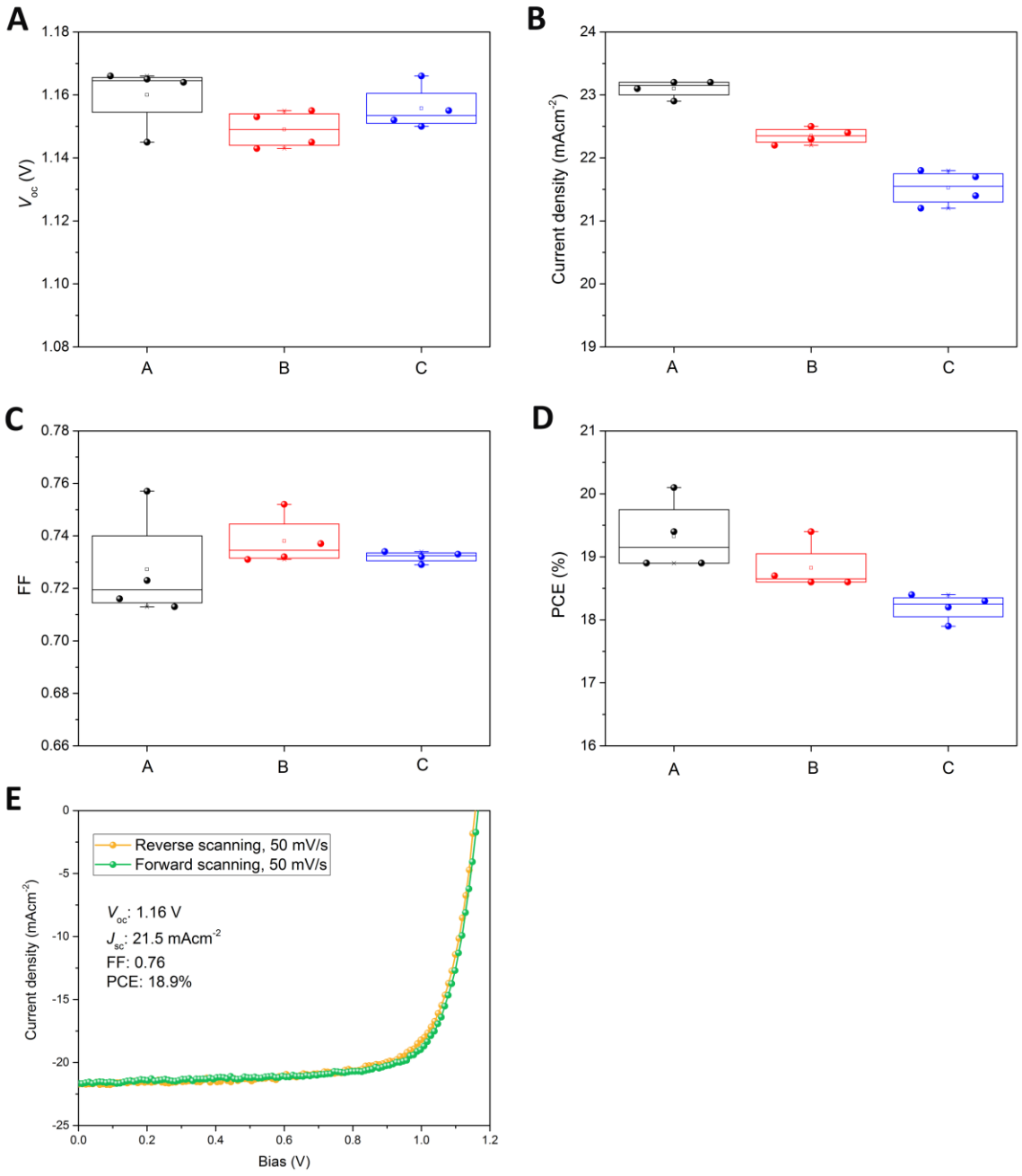

Fig. S3. Photovoltaic performance of single-junction perovskite solar cells. Statistics of the photovoltaic performance metrics of opaque perovskite solar cells fabricated with different perovskite thicknesses (**A**) 470 ± 20 nm, (**B**) 380 ± 20 nm, and (**C**) 310 ± 20 nm. (**E**) Reverse and forward scanning *J*-*V* behavior of opaque single-junction perovskite solar cells (perovskite thickness: 310 ± 10 nm) tested on a FTO substrate.

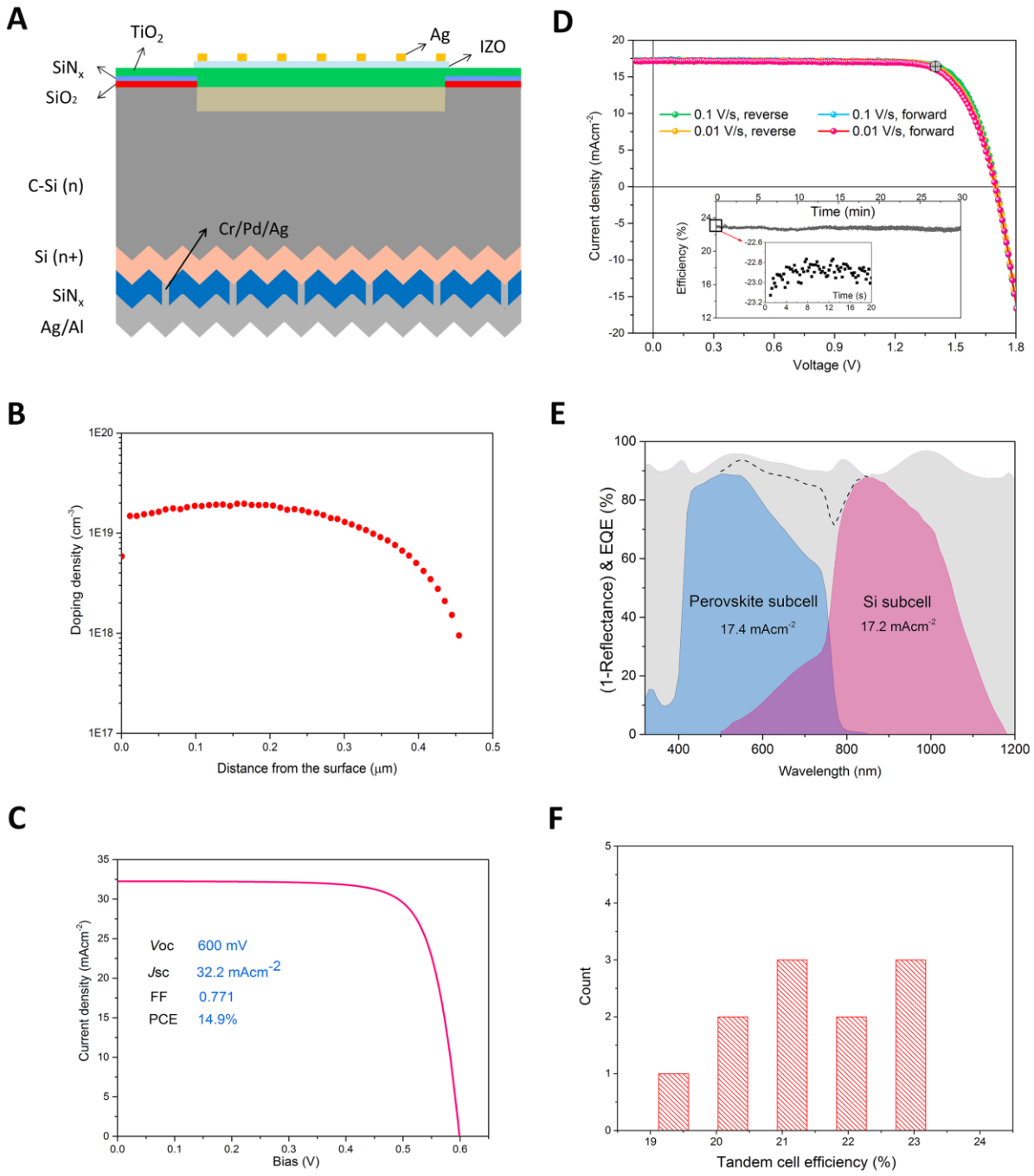

Fig. S4. Structure and photovoltaic performance of Si homojunction device and corresponding tandem device. (**A**) Schematic of single-junction Si homojunction solar cell including ALD-TiO_2 on a flat p^+-Si emitter (not to scale). (**B**) Doping profile of the p^+-Si doping for Si subcell as obtained from electrochemical capacitance vs voltage (ECV) measurements. (**C**) *J-V* behavior of a single-junction homojunction Si solar cell. (**D**) *J-V* behavior of the proof-of-concept tandem device with both reverse and forward scanning at 0.05 V/s based on Si homojunction subcell. (**E**) Absorbance (1-R, where R is the reflectance) of the tandem device (grey shading), EQE of the perovskite top cell (blue), and EQE of the c-Si bottom sub-cell (red). (**F**) Statistics of the efficiency for eleven tandem solar cells based on homojunction Si subcell from three separate batches of fabrication.

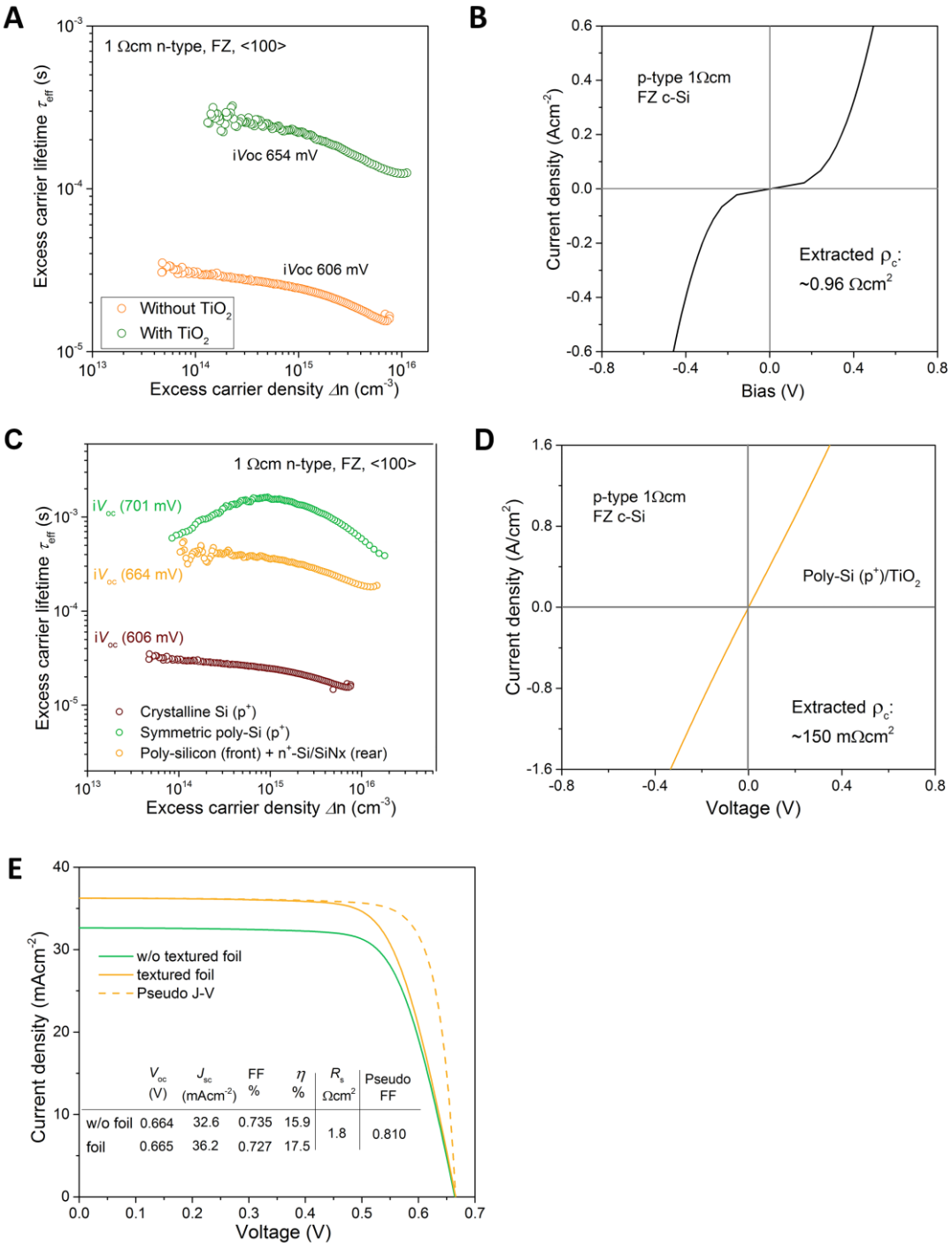

Fig. S5. Passivation and contact behaviors with optimized TiO_2 film and poly-Si substrate. (**A**) Excess carrier lifetime of a p^+-Si substrate with and without TiO_2 passivation ($TiCl_4$-ALD TiO_2 deposited at 150 °C without further annealing) as a function of the measured injection level. The implied V_{oc} (iV_{oc}) is increased by ~50 mV with the $TiCl_4$ TiO_2 coating. (**B**) *J-V* curve of a $TiCl_4$-ALD (150 °C) TiO_2/p^+-Si sample (p^+-Si has a doping density of ~$1.5*10^{19}$ cm^{-3}). (**C**) Excess carrier lifetime as a function of excess carrier density for a Si substrate with a symmetric p^+-Si homojunction (red), symmetric poly-Si (green), and poly-Si front/SiN_x rear (yellow). These lifetimes have an implied V_{oc} of 606 mV, 701 mV, and 664 mV, respectively. (**D**) *J-V* curve of a $TiCl_4$-ALD TiO_2 (deposited at 200 °C) /poly-Si sample. (**E**) *J-V* curves of a single-junction poly-Si solar cell with and without textured foil on the front side, and the pseudo *J-V* curve indicating a high pseudo-*FF* of 0.810.

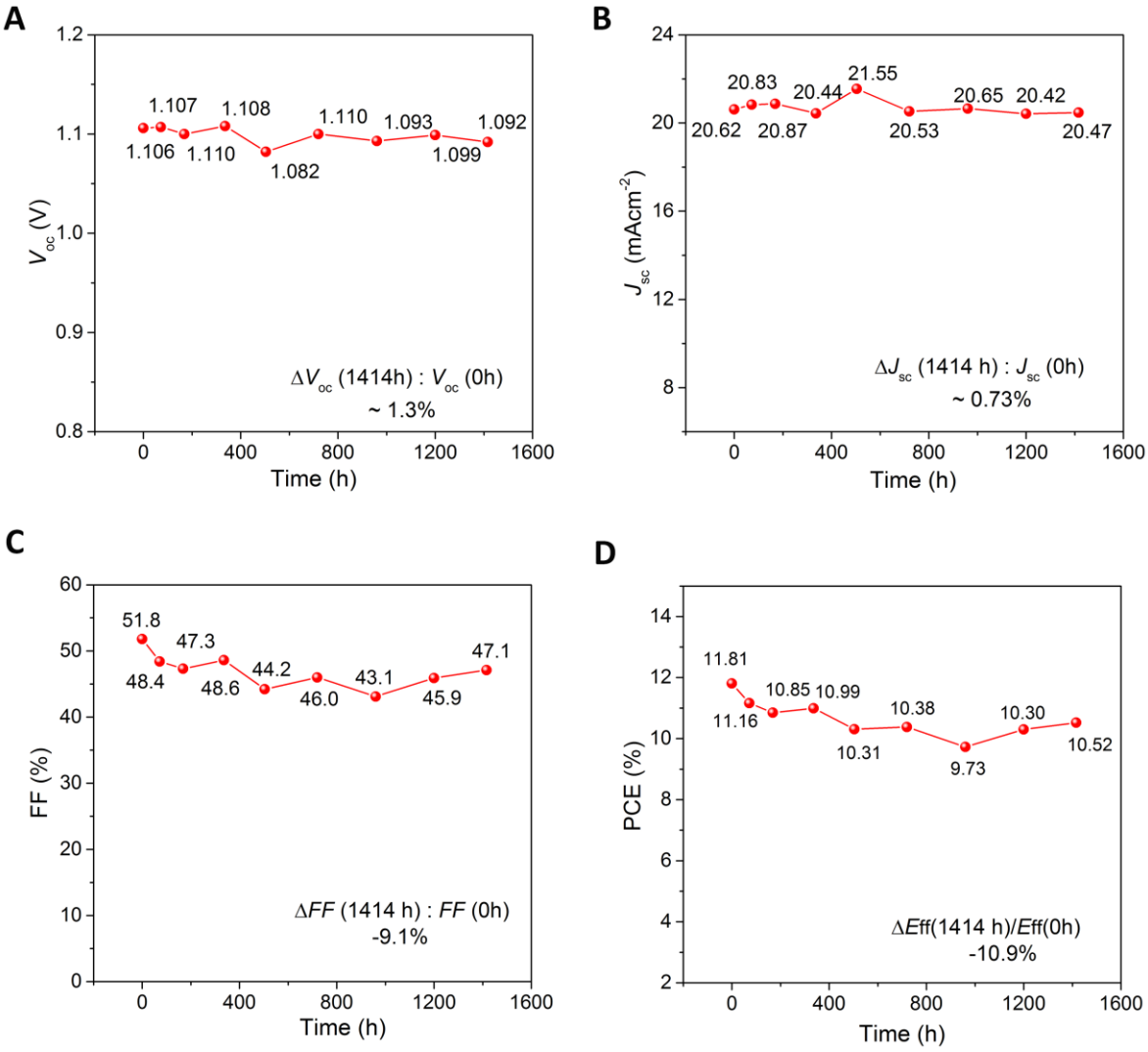

Fig. S6. Damp heat test of an encapsulated semitransparent perovskite solar cell. Evolution of the photovoltaic characteristics including (**A**) V_{oc}, (**B**) J_{sc}, (**C**) FF and (**D**) PCE during damp heat stability of an encapsulated single-junction perovskite device for 1414 h. (Test condition: 85 °C in a relative humidity level of 85%)

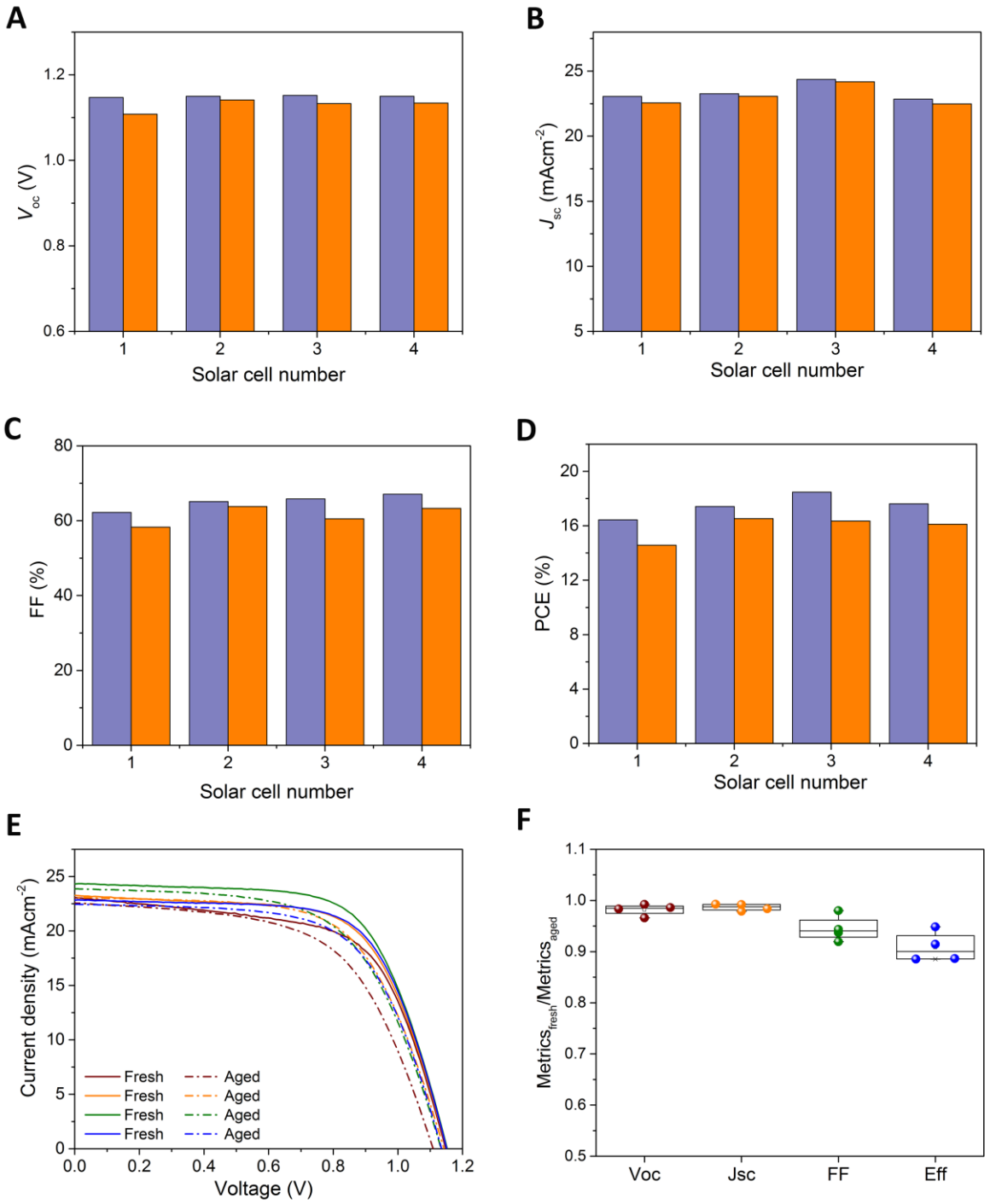

Fig. S7. Histogram of stability test for four perovskite solar cells. The changes in (**A**) V_{oc}, (**B**) J_{sc}, (**C**) FF, (**D**) PCE, and (**E**) *J-V* behavior for four non-encapsulated semi-transparent perovskite solar cells after 85 °C heating for 24 h in the dark. The purple column represents the performance of the new, as-fabricated device, and the yellow column shows the yield after the aging process. (**F**) Shows the statitics of the ratio of the fresh cell performance to that of the aged cell for the V_{oc}, J_{sc}, FF, and PCE. A ratio of 1 indicates no change before and after testing.

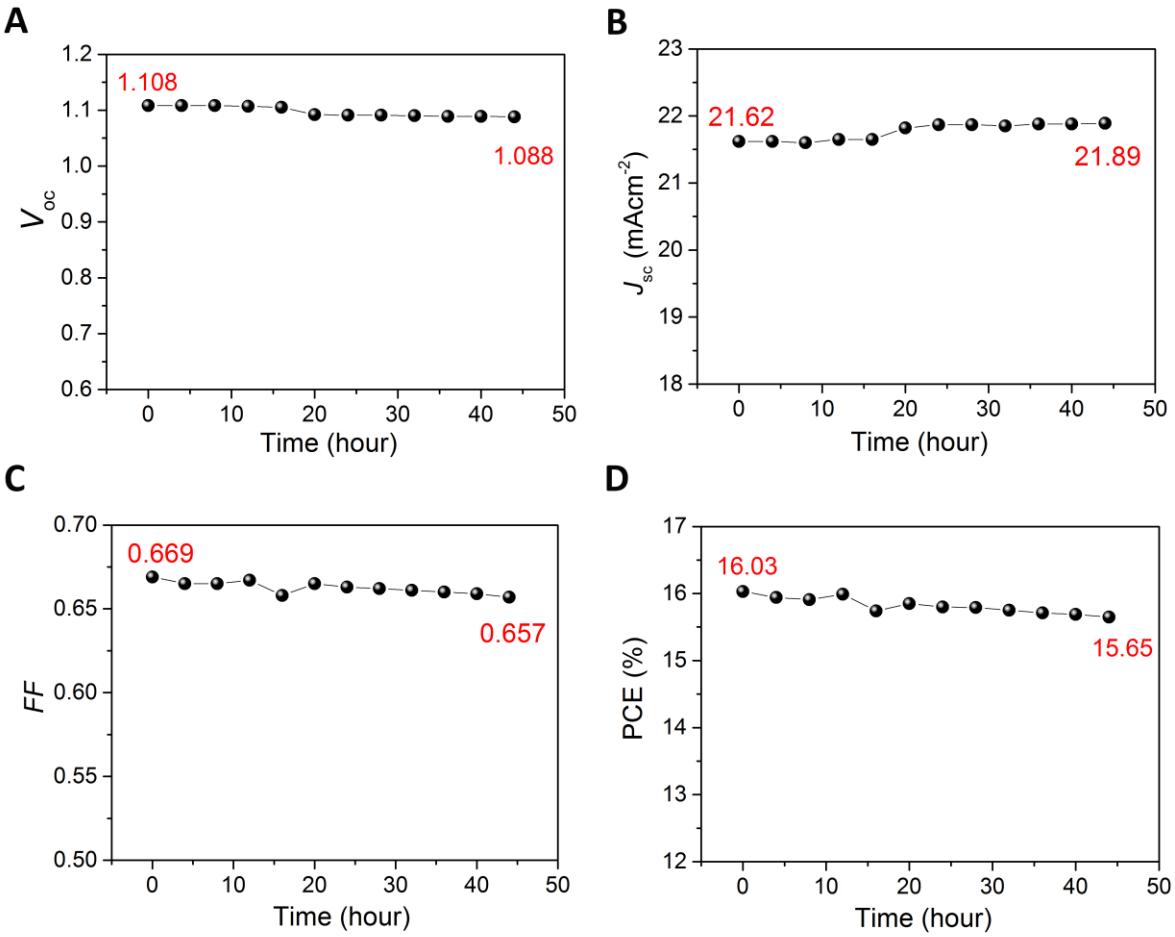

Fig. S8. Light-soaking: Irradiance test of perovskite solar cell. Photovoltaic metrics (**A**) V_{oc}, (**B**) J_{sc}, (**C**) FF, and (**D**) PCE evolution of a single-junction perovskite solar cell under continuous 1-Sun illumination (100 mW cm^{-2}, including UV radiation) for 44 h controlled at 60°C. The total irradiance exceeds the requirement of at least 43 KWh/m^2 defined in IEC 61646.

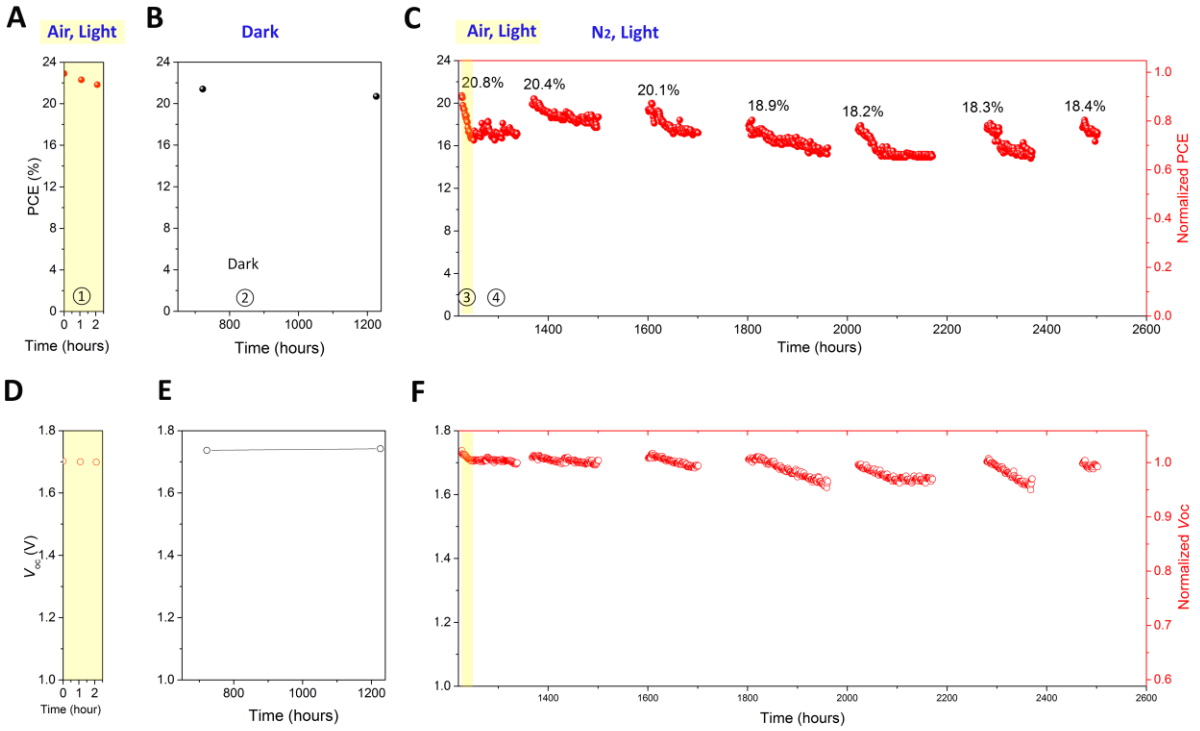

Fig. S9. Stability test of nonencapsulated perovskite/Si tandem solar cell. PCE evolution of the proof-of-concept perovskite/Si tandem device undergoing four different aging stages. (**A**) Stage 1: 1 Sun continuous illumination in air for ~2.1 h, biased near maximum power point); (**B**) Stage 2: device stored in dark in a N_2 cabinet for ~1224 h; (**C**) Stage 3: device under 1 Sun continuous illumination in air for ~19 h, biased at ~1.3 V, and Stage 4: device underwent light/dark cycles for seven cycles, with total illumination of over 800 h. The measurement under light was taken at 25 °C. Corresponding V_{oc} evolution (**D**-**F**) of the same device under the same conditions.

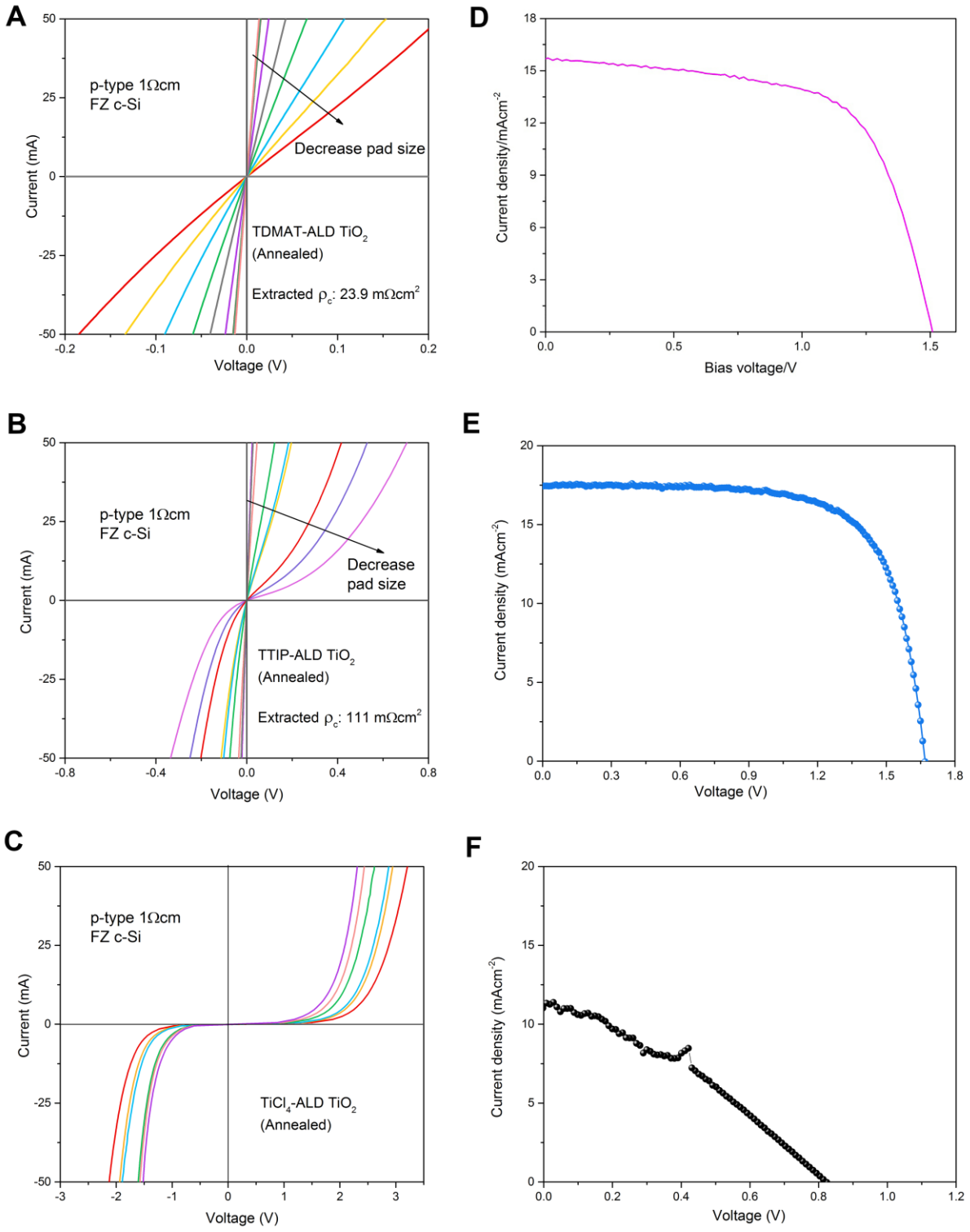

Fig. S10. Contact behavior of p-Si and various TiO_2 films and *J-V* curves of corresponding tandem devices. *I-V* data for (**A**) a TDMAT-ALD TiO_2/p^+-Si sample, (**B**) a TTIP-ALD TiO_2/p^+-Si sample and (**C**) a $TiCl_4$-ALD (75 °C) TiO_2/p^+-Si sample with different pad sizes. All samples were annealed at 400 °C under ambient conditions with different pad sizes, and annealed at 400 ℃ under ambient conditions. *J-V* curve of a 2-T perovskite/Si tandem device based on (**D**) ITO as the recombination layer, and with in situ recombination junction using (**E**) TTIP-ALD TiO_2, and (**F**) $TiCl_4$–ALD TiO_2 (deposited at 75°C).

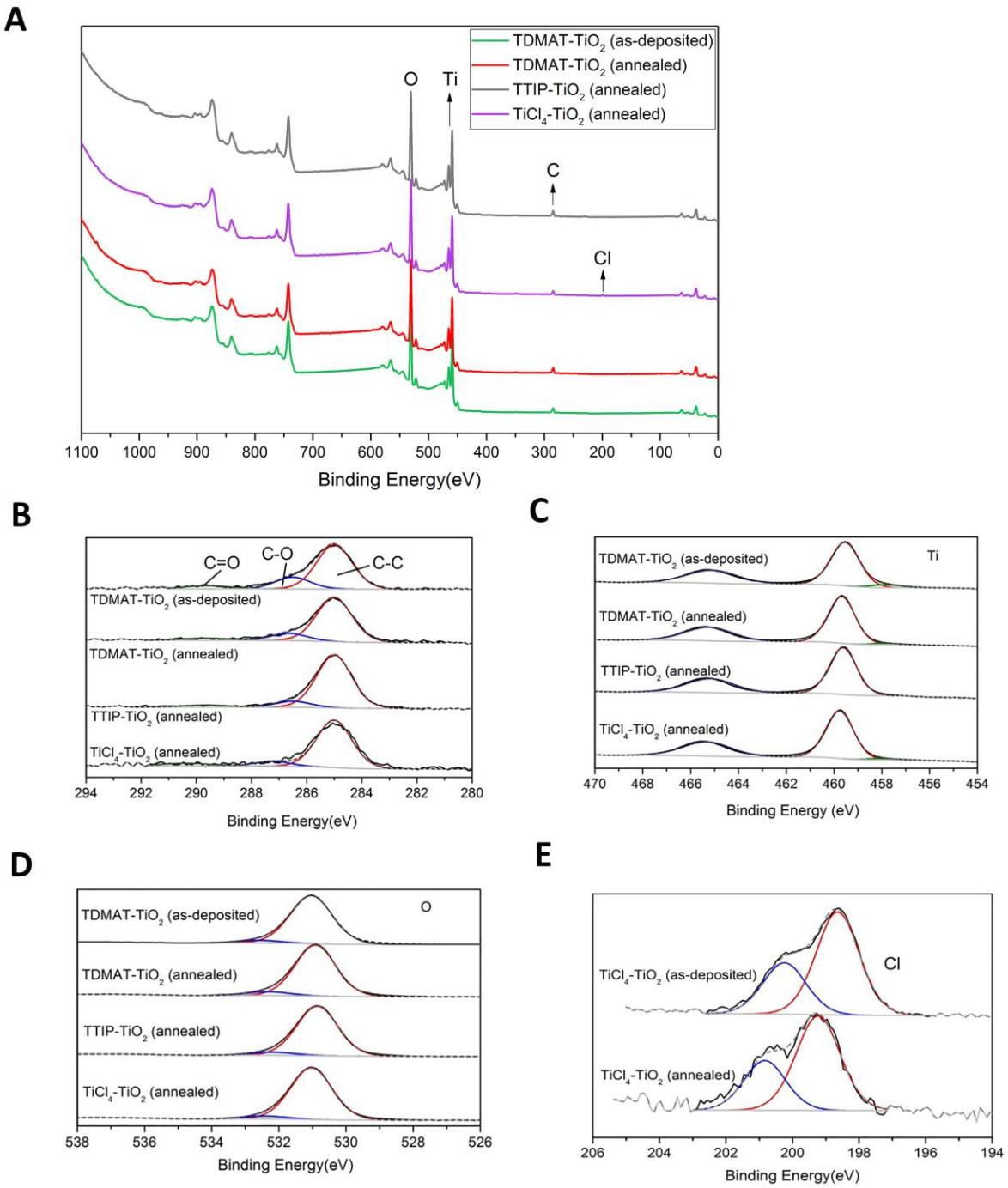

Fig. S11. XPS analysis of different TiO_2 films fabricated with different ALD precursors. XPS survey scans for TDMAT-ALD TiO_2 (as-deposited and annealed), TTIP-ALD TiO_2 (annealed) and $TiCl_4$-ALD TiO_2 (annealed) samples. Core photoelectron spectra of (**B**) C 1s (**C**) Ti 2p (**D**) O 1s for TDMAT-ALD TiO_2 (as-deposited), TDMAT-ALD TiO_2 (annealed), TTIP-ALD TiO_2 (annealed) and $TiCl_4$-ALD TiO_2(annealed) samples, and that of (**E**) Cl 2p from a $TiCl_4$-ALD TiO_2 (annealed and as-deposited) sample. Note here, the $TiCl_4$-ALD TiO_2 was deposited with a reactor temperature of 75 °C.

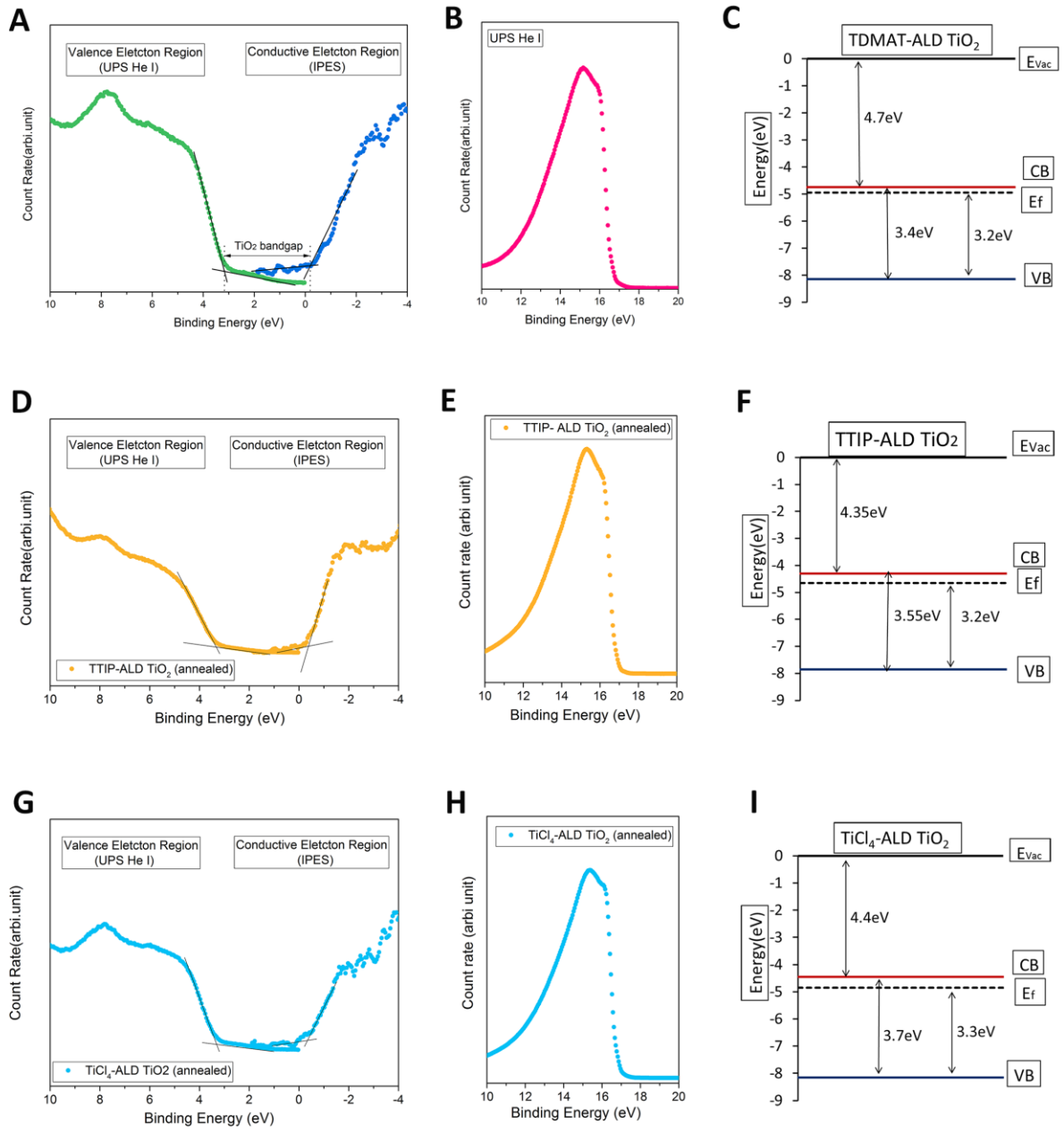

Fig. S12. Energy level analysis of TiO_2 films fabricated with different precursors. (**A**) Combined UPS valence band spectrum and IPES, and (**B**) the secondary electron cut-off region, and (**C**) calculated energy diagram from the above measurement, of an annealed TDMAT-ALD TiO_2 layer. The error for the work function was ±0.2 eV, and the extraction of valence band and conduction band had an error of ±0.1 eV. (**D**) Combined UPS valence band spectrum and IPES, and (**E**) the secondary electron cut-off region representative, and (**F**) calculated energy diagram from the above measurement of an annealed TTIP-ALDTiO_2 layer. (**G**) Combined UPS valence band spectrum and IPES, and (**H**) the secondary electron cut-off region representative, and (**I**) calculated energy diagram from the above measurement of an annealed $TiCl_4$-ALD TiO_2 layer (deposited at 75°C).

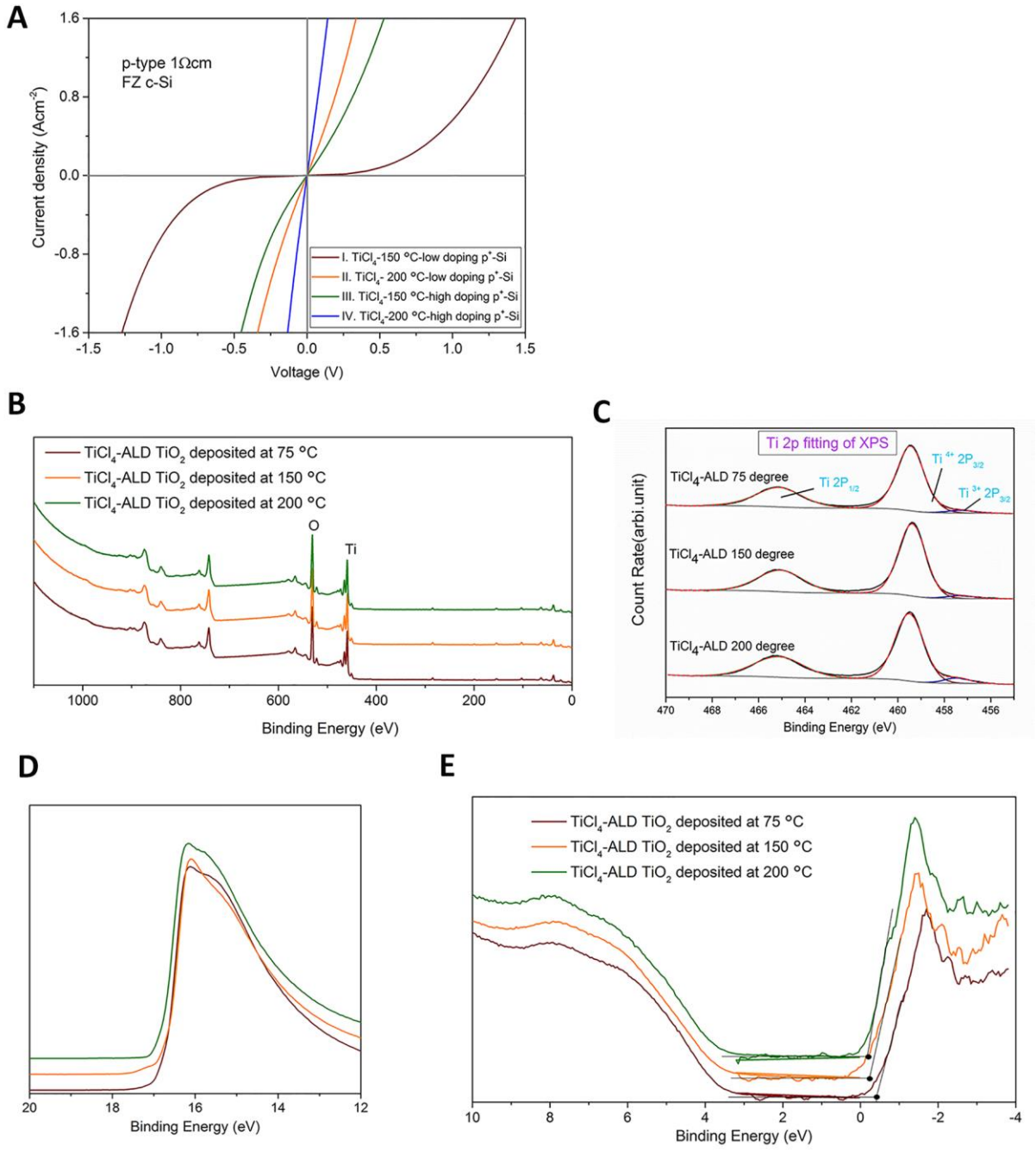

Fig. S13. Contact behavior and energetics analysis of $TiCl_4$-ALD TiO_2 films deposited at different temperatures. (**A**) *J-V* curves of the $TiCl_4$-ALD TiO_2 deposited at low temperatures on different p^+-Si wafers. The samples receive no further heat-treatment. TiO_2 deposited at 150°C on top of p^+-Si with a doping density of (I) ~9.3×10^{19} cm^{-3}, the extracted contact resistivity is ~850 $m\Omega cm^2$ and (III) ~1.7×10^{20} cm^{-3}, the extracted contact resistivity is ~445 $m\Omega cm^2$. TiO_2 deposited at 200°C on top of p^+-Si with a doping density of (II) ~9.3×10^{19} cm^{-3}, the extracted contact resistivity is ~210 $m\Omega cm^2$ and (IV) ~1.7×10^{20} cm^{-3}, the extracted contact resistivity is ~99.6 $m\Omega cm^2$. Energetics of $TiCl_4$-ALD TiO_2 layers deposited at 75°C, 150°C and 200°C without further annealing: (**B**) XPS survey scans. (**C**) Ti 2p core-level photoemission. The proportion of Ti^{3+} increases with the $TiCl_4$ deposition temperature. (**D**) The secondary electron cut-off region. (**E**) Combined UPS valence band spectra and IPES. From IPES, the fermi-level to conduction-band separations of the TiO_2 deposited at 75°C, 150°C and 200°C are calculated to be ~0.4 eV, ~0.3 eV and ~0.2 eV, respectively.

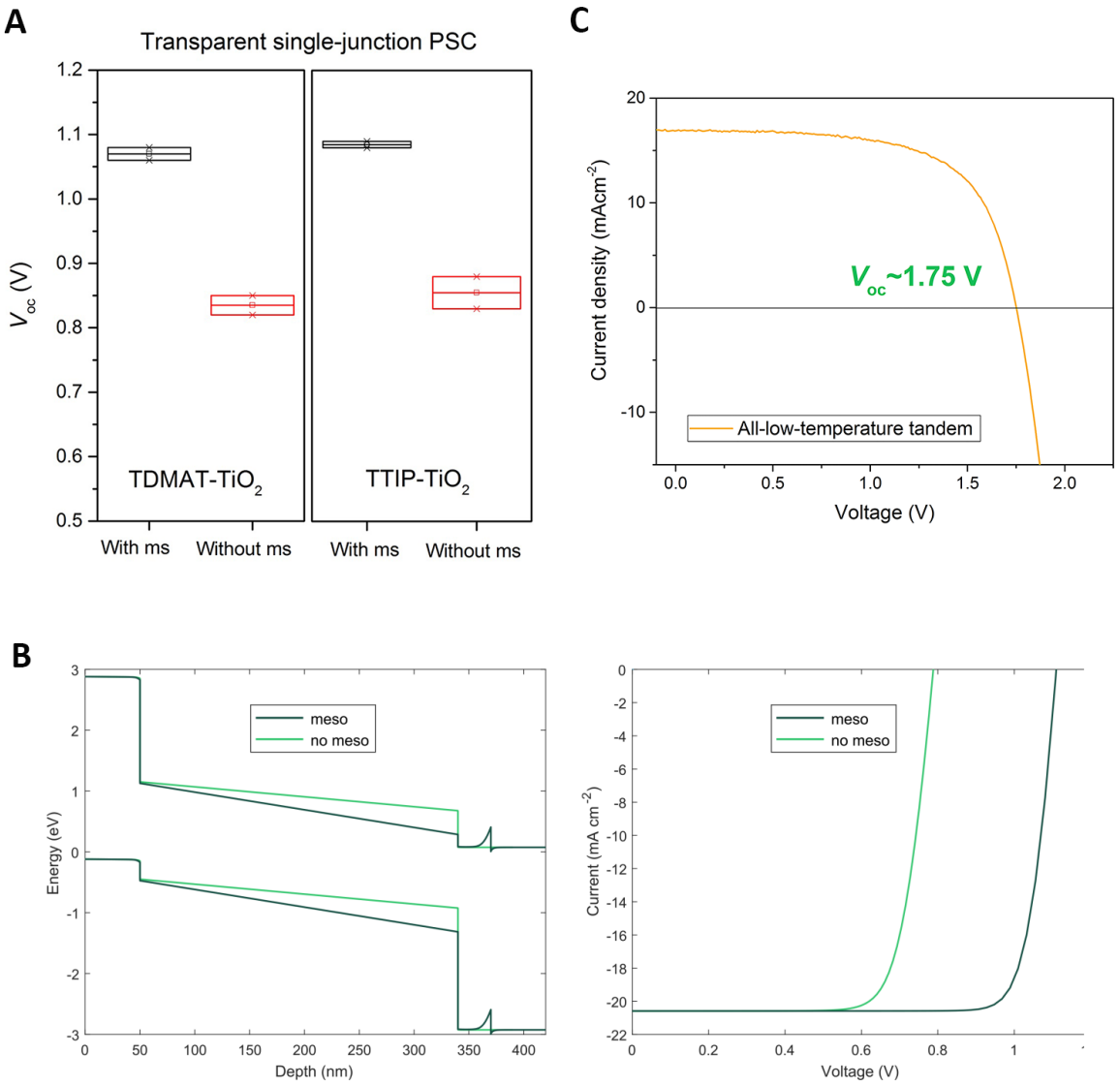

Fig. S14. Effect of ms-TiO_2 on the performance of different tandem devices. (**A**) V_{oc} yield of transparent single-junction perovskite solar cells (with p^+-Si as the substrate) with and without mesoporous-TiO_2. Results for TDMAT-ALD TiO_2 are shown on the left while results for TTIP-ALD TiO_2 are shown on the right. Both titania compact layers have high work functions with the deposition conditions used in this work. (**B**) Simulated band diagram at 0 V (left) and *J-V* behavior (right) of a single-junction perovskite solar cell with and without an additional "mesoporous" titania layer inserted between the perovskite and high work-function compact titania. This represents a 1D simplification of the complex 3-dimensional mesoporous structure present in our tandem cell design, but captures the qualitative effect of including titania layers with contrasting work functions. The mesoporous layer functions primarily to maintain the built-in voltage in the perovskite cell, as seen in the band diagram (left) and consequently discrepant open-circuit voltages (right). Here electron affinities of 4.1 eV and 4.5 eV were used for the compact and mesoporous titania layers respectively. (**C**) *J-V* curve of a monolithic perovskite/Si tandem solar cell with as-deposited $TiCl_4$-ALD TiO_2 (200 °C). The top perovskite subcell has a planar structure without the inclusion of the mesoporous TiO_2 film, and is fabricated with low-temperature processes.

Table S1. Hysteresis behavior of a tandem device. Photovoltaic metrics of the 2-T perovskite/Si tandem device based on TDMAT-ALD TiO_2, extracted from *I-V* data scanned at 0.1 V/s and 0.01 V/s under both reverse and forward scanning, respectively. Si homojunction solar cell is used as the bottom subcell.

Scan rate	**Scan direction**	**V_{oc} (mV)**	**J_{sc} ($mAcm^{-2}$)**	**FF**	**PCE (%)**
0.1V/s	RS	1703	17.2	0.792	23.2
	FS	1698	17.1	0.789	22.9
0.01 V/s	RS	1704	17.2	0.782	22.9
	FS	1697	17.1	0.779	22.6

Table S2. Electrical properties of as-deposited TiO_2. Hall-effect measurements for as-deposited TDMAT-ALD TiO_2.

Field [G]	Resistivity [ohm cm]	Hall Coefficient [cm^3/C]	Type	Carrier Density [$1/cm^3$]	Hall Mobility [$cm^2/(VS)$]
$1.0000x10^3$	$1.5740x10^2$	$-1.6028x10^1$	n	$3.8947x10^{17}$	$1.0449x10^{-1}$
$3.0000x10^3$	$1.5720x10^2$	$-1.5976x10^1$	n	$3.9071x10^{17}$	$1.0416x10^{-1}$
$5.0001x10^3$	$1.5678x10^2$	$-1.9460x10^1$	n	$3.2078x10^{17}$	$1.2686x10^{-1}$

Table S3. Electrical properties of annealed TiO_2. Hall-effect measurements for annealed TDMAT-ALD TiO_2.

Field [G]	Resistivity [ohm cm]	Hall Coefficient [cm^3/C]	Type	Carrier Density [$1/cm^3$]	Hall Mobility [$cm^2/(VS)$]
$1.0000x10^3$	$8.4670x10^{-1}$	$-8.2446x10^{-1}$	n	$7.5713x10^{18}$	$9.8962x10^{-1}$
$3.0000x10^3$	$8.4615x10^{-1}$	$-7.8738x10^{-1}$	n	$7.9278x10^{18}$	$9.4511x10^{-1}$
$5.0001x10^3$	$8.4497x10^{-1}$	$-7.8614x10^{-1}$	n	$7.9403x10^{18}$	$9.5362x10^{-1}$

Simulation Information

Analysis of the SRH model

Valuable insights can be gained by imposing some simplifying assumptions on the SRH model introduced in the main text. Assuming that a single SRH defect is present at the interface, the heterojunction current can then be expressed in terms of the SRH equation:

$$j = \frac{e\,(np - n_0 p_0)}{v_n^{-1}(p + p_t) + v_p^{-1}(n + n_t)}$$

where n, p are the carrier densities at the interface (electrons on the n-side and holes on the p-side respectively), n_0, p_0 are their respective equilibrium values, v_n, v_p are the quasi-recombination velocities, and n_t, p_t are related to the defect energy level [1]. Assuming further that the carrier mobilities are high enough to result in essentially flat quasi-fermi levels throughout the interfacial region, this relationship can be further related to the applied voltage V as:

$$j = \frac{e\,N_c N_v \exp\left(-\frac{\Delta}{v_{th}}\right)\left(\exp\left(\frac{V}{v_{th}}\right) - 1\right)}{v_n^{-1}\left(N_A \exp\left(-\frac{V_p}{v_{th}}\right) + p_t\right) + v_p^{-1}(N_D \exp\left(-\frac{V_n}{v_{th}}\right) + n_t)}$$

in which $v_{th} = {kT}/{e}$, $V_{p,n}$ denote the potential drops in the n and p-side depletion regions ($V_n + V_p = V_{bi} - V$), $N_{A,D}$ are the donor and acceptor doping densities on the n- and p-side respectively and $N_{c,v}$ the density of states. The expression simplifies somewhat for the small-signal conductivity to

$$\sigma = \frac{dj}{dV}\Big|_{V=0} = \frac{\frac{e}{v_{th}} N_c N_v \exp\left(-\frac{\Delta}{v_{th}}\right)}{v_n^{-1}(p_0 + p_t) + v_p^{-1}(n_0 + n_t)}. \qquad (S1)$$

An extremum occurs with respect to the placement of the equilibrium Fermi level E_{f0} within the interfacial band gap Δ (assuming V_{bi} is fixed) when $v_n n_0 = v_p p_0$, i.e. σ is maximized when the interfacial carrier densities are *balanced* in the stated sense. This conclusion applies regardless of whether the interface defects carry a substantial charge. Defects of donor type partially compensate the acceptor p-side doping, and therefore require larger acceptor doping to reach the optimum balance than if the defect charge were absent (c.f. the comparison between neutral and donor defects in Fig. 4B of the main text). Conversely, acceptor-type defects compensate the n-side donor doping and shift the balance towards requiring extra donors.

SCAPS parameters

	E_g (eV)	χ (eV)	μ_n ($cm^2V^{-1}s^{-1}$)	μ_p ($cm^2V^{-1}s^{-1}$)	N_c (cm^{-3})	N_v (cm^{-3})	*width* (nm)	$N_A - N_D$ (cm^{-3})	ϵ_r
n-side (TiO_2)	3.0	4.27-477 (4a), 4.67 (4b)	0.5	0.5‡	10^{20}	10^{20}	50	-10^{18}	31
p-side (p-Si)	1.12	4.05	1500‡	450	$2.8x10^{18}$ [7]	10^{19} [7]	100	10^{19} (4a), 10^{17} - 10^{20} (4b)	12

‡The neglect of absorption in the transport layers makes these minority carrier mobilities of little to no importance.

	Type	Central Energy Level	Gaussian Width (σ)	Density (cm^{-2})	Capture Cross-Sections (cm^{-2})
Interface Defect	Neutral (4a,b), Donor (4b), Acceptor (4b)	Mid-gap	0.15 eV	10^{13} (4a), $4x10^{13}$ (4b)	$\sigma_n = \sigma_p = 10^{-15}$ (4a) $\sigma_n = \sigma_p = 5x10^{-17}$ (4b)

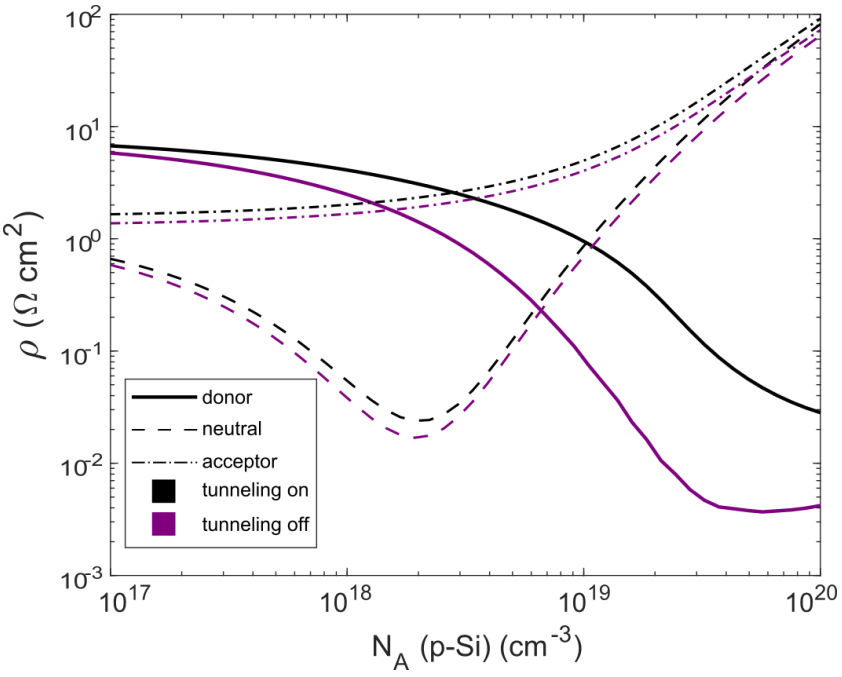

Fig. S15. Simulation of the effect of tunneling on the contact behavior. Calculated small-voltage resistivity as in Fig. 4B of the main text, this time showing the effect of tunneling. Tunneling has a minor effect for neutral and acceptor-type defects, but significantly affects the donor-defect models when the acceptor doping is large because tunneling effects are most significant when the depletion region is small which occurs for large acceptor doping concentrations.